Thin-Walled Structures 171 (2022) 108686

Contents lists available at ScienceDirect

Thin-Walled Structures

journal homepage: www.elsevier.com/locate/tws

Full length article

Topography and size optimization of composite structure to control buckling temperature and thermal buckling mode shape

Hoo Min Lee [a], Kang Kuk Lee [b], Gil Ho Yoon [a,*]

[a] School of Mechanical Engineering, Hanyang University, Seoul, South Korea
[b] Department of Research and Development, Hyundai Mobis, Yongin, South Korea

ARTICLE INFO

Keywords:
Topography optimization
Size optimization
Buckling temperature
Buckling mode
Thermal buckling
Composite structure

ABSTRACT

Composite material has been widely used in the engineering field because of its excellent fatigue and corrosion resistance and good impact resistance. However, the structural instability of composite structure is observed due to the thermal buckling phenomena when applied with heat. The present study aims to achieve the thermal structural stability of composite plate structure by developing a topography optimization method and a size optimization method to control linear buckling temperature and thermal buckling modes. In this study, the nodal positions or the shell element thicknesses are set as the design variables. The buckling temperature values and buckling mode shapes are included in the objective function. The developed optimization methods determine the optimal thickness distributions and geometries of composite structure, to induce the target buckling temperatures and target buckling mode shapes. To demonstrate the validity of the present approach, several structural optimization problems considering composite plates are solved. The proposed optimization methods allows the convergence of buckling temperatures within 1% range, and that of buckling mode shapes to desired geometries. In addition, the engineering application of the optimization method on reaction turbine blade is presented. The results of this study support the implementation of the topography and size optimization methods to achieve the optimum structural designs for various engineering applications regarding buckling temperature and thermal buckling mode shape.

1. Introduction

Composite material has been widely used in the engineering fields such as aerospace, mechanical, electrical, bio-medicine and military engineering because of its excellent fatigue and corrosion resistance and good impact resistance [1]. With increasing demand, various materials and manufacturing methods have been utilized and developed to manufacture composites. Materials such as carbon fiber, epoxy, metals, and plastic resin have been involved in prepregging process [2], cladding of metal components [3], and fused deposition methods [4] to manufacture various composite materials. Fig. 1 shows the examples of composite structures in real life, manufactured using the listed methods. Yet, composite materials do show some limitations in certain aspects, and one of the limitations of composite materials is the structural instability caused by thermal buckling phenomena when applied with heat. The present study aims to achieve structural stability of composite structures at external thermal conditions. As finite element method (FEM) can be used to accurately predict buckling distortion [5] and conduct buckling analysis of composite plates with combined thermal and mechanical loads [6], this study develops topography and size optimization methods using finite element simulations of composite structure to control the linear buckling temperature and thermal buckling modes. According to the buckling theory, geometric features affect the buckling temperature and buckling modes of the structures. Thus, this study sets the node positions (topography optimization) and element thicknesses (size optimization) as the design variables, by applying the FEM. The buckling temperature and buckling mode shapes are included in the objective function. To validate the present optimization methods, several optimization examples including plate and turbine blade are solved, to control the buckling temperature and buckling mode shapes.

The structural instability, arising from the buckling phenomenon under various thermal conditions, has been an important and widely investigated issue in engineering fields. The analyses of thermal buckling and instability of porous plates [7], a coupling of the thermoelastic instability and buckling in automotive clutches [8], an investigation of beam instability under thermal loading [9], and studies on the dynamic instability of multi-layer beams in thermal environments [10] have been conducted to analyze the structural instability. Nonlinear bending analysis of porous micro tubes based on modified couple stress

* Corresponding author.
E-mail address: ghy@hanyang.ac.kr (G.H. Yoon).

https://doi.org/10.1016/j.tws.2021.108686
Received 15 July 2021; Received in revised form 29 October 2021; Accepted 17 November 2021
Available online 8 December 2021

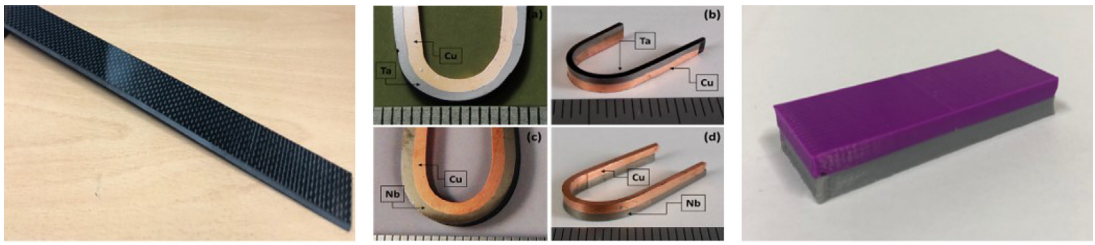

Fig. 1. Composite materials: (a) Carbon–epoxy plate, (b) Tantalum and Niobium coated with copper (Courtesy by MELD Manufacturing Corporation via http://meldmanufacturing.com/coat/), and (c) 3D printed structure.

theory [11] and buckling analysis of smart beams based on higher order shear deformation theory [12] have been conducted to apply various theories in the analyses of nonlinear deformation issues. Studies on the influence of temperature change on column buckling [13], thermo-mechanical buckling of cylindrical panels [14], temperature distribution effects on the buckling behavior [15], and thermal buckling of thin composite plates [16] have been conducted to investigate the effects of temperature on the buckling issues. Studies on the column buckling of structural bamboo [17], local buckling of structural steel shapes [18], and design of composite wings for buckling constraints [19] have been conducted to investigate the effects of the structural design on the buckling problems. Studies on the influence of the material composition on the buckling response [20] and the effect of plates with internal discontinuities on the buckling [21] have been investigated to determine the effects of the material composition on the buckling issues. A thermal buckling analysis of porous plates [22], an investigation of the surface and thermal load effects on the buckling of the nanowires [23], research on the buckling of thick plates under thermal loads [24] and buckling behavior of the plates under non-uniform thermal loads [25] have been conducted to understand the thermal buckling issues. Despite the remaining uncertainties that lead to structural instability, buckling phenomenon has been applied in various engineering fields that require intentionally large deformations within a short period of time. Buckling has been used to trigger the movements of programmable soft robots and actuators [26–28]. The motion of flexible structures and wearable electronics has been triggered using buckling in recent studies [29–31]. The transformation of origami-inspired structures has been actuated using the buckling phenomenon [32–36]. The increasing demand for buckling in various engineering applications has increased the need to control unpredictable phenomena. Reviewing the relevant studies, various numerical methods have been developed and applied to solve the buckling problems. Studies on topology optimization [37,38] and section thickness optimization [39] considering thermal buckling have been conducted. However, the results of such studies have shown limitations in direct application to engineering fields, as structural designs with non-continuous thickness variations are induced. The current engineering field requires a practical optimization scheme that considers thermal buckling, which can be directly applied to the structural optimization problems. Thus, this study aims to develop optimization frameworks, determining continuous thickness variations as well as topography while optimizing the buckling temperature and buckling mode shape.

In the present topography and size optimization, the location of nodes or thickness of shell elements are set as the design variables, as shown in Fig. 2. In the topography optimization method, the locations of the nodes in the out-of-plane direction are used as the design variables. As the structural stiffness varies from the perturbation of the coordinate values of the nodes, it is possible to change and optimize the buckling temperature and buckling mode. In the size optimization method, the thickness values of the shell elements at each node are varied. The thickness values inside the shell element vary according to the assigned thickness values of the corresponding nodes, which are perturbed from the mid-plane. The perturbed design variables affect the stiffness matrix of the structure as well as the linear buckling temperature and buckling mode shapes. The difference between the buckling and target buckling temperatures and that between the buckling and target buckling modes are set as the objective functions. To consider the cost, the volume of the structure is bounded. An FEM analysis with a 181-shell element in ANSYS and a gradient-based optimization algorithm in MATLAB are employed for the present topography and size optimization methods. With the present optimization schemes, it is possible to acquire the optimal designs of composite structure with desired buckling temperature values and buckling mode shapes. Several optimization problems considering composite plates are solved using the present frameworks, to validate their efficiency and accuracy. In addition, the engineering application of the optimization method on reaction turbine blade is presented. Regardless of the structural complexity, and the presence of heat dissipation and centrifugal force, structural stability of the blade is achieved. The results in this study supports the application of the proposed structural optimization method on various engineering applications to solve structural instabilities present in thermal buckling cases.

The remainder of this paper is organized as follows. Section 2 provides the theoretical background for the eigen-buckling analysis and optimization formulation. Section 3 provides several structural optimization examples, considering the buckling temperatures and buckling mode shapes. Section 4 presents the application of the present optimization scheme to some practical examples, considering the thermal buckling of steam turbine blades. Finally, some concluding remarks and future research topics are discussed in Section 5.

2. Optimization formulation

2.1. Linear eigen-buckling analysis

Linear eigenvalue buckling analysis using four-node shell elements is conducted in this study, because shell structures experience several buckling cases among 3D structures [40,41]. The shape functions of the four-node shell element are formulated as follows.

$$N_1 = \frac{1}{4}(1-\xi)(1-\eta),\ N_2 = \frac{1}{4}(1+\xi)(1-\eta)$$
$$N_3 = \frac{1}{4}(1+\xi)(1+\eta),\ N_4 = \frac{1}{4}(1-\xi)(1+\eta) \tag{1}$$

The isoparametric space is defined as $\xi-\eta$. To obtain the stiffness matrix, the strain–displacement matrix, $\mathbf{B}$, is defined as follows.

$$\mathbf{B} = \begin{bmatrix} \bar{\mathbf{B}}_1 & \bar{\mathbf{B}}_2 & \bar{\mathbf{B}}_3 & \bar{\mathbf{B}}_4 \end{bmatrix},$$
$$\bar{\mathbf{B}}_n = \begin{bmatrix} N_{n,\xi} & 0 & 0 & 0 & 0 & 0 \\ 0 & N_{n,\eta} & 0 & 0 & 0 & 0 \\ N_{n,\eta} & N_{n,\xi} & 0 & 0 & 0 & 0 \\ 0 & 0 & 0 & 0 & N_{n,\xi} & 0 \\ 0 & 0 & 0 & N_{n,\eta} & 0 & 0 \\ 0 & 0 & 0 & N_{n,\xi} & N_{n,\eta} & 0 \end{bmatrix} \tag{2}$$

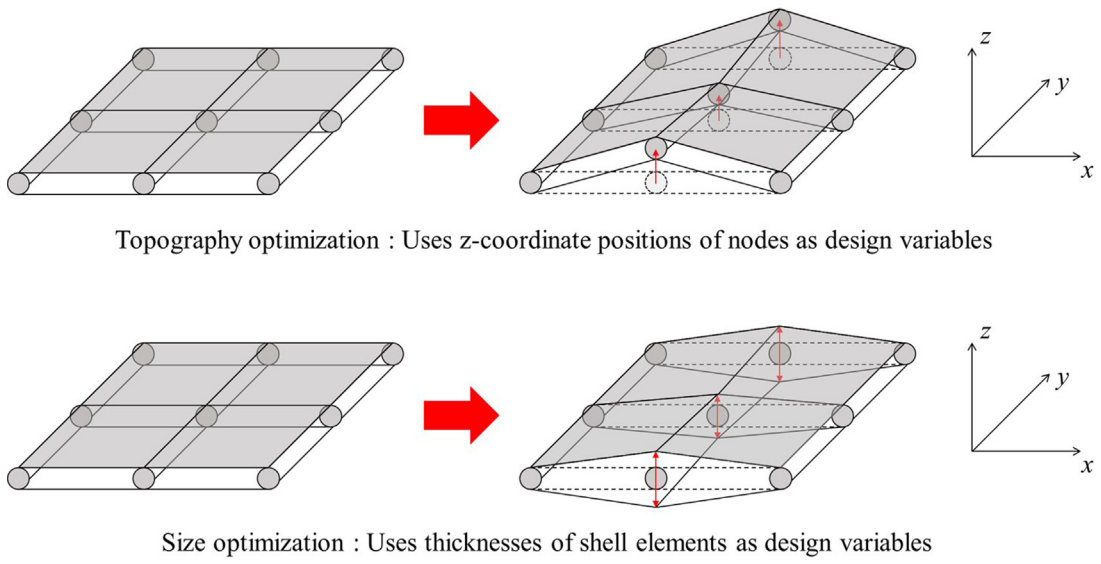

Fig. 2. Illustration of topography and size optimization mechanism.

The strain–displacement matrix, **B**, is composed of the derivatives of the shape functions. The shell element constitutive matrix, **D**, is expressed as follows.

$$\mathbf{D} = \frac{E}{(1-\nu^2)}\begin{bmatrix}\bar{\mathbf{D}} & 0\\ 0 & \frac{h^3}{12}\bar{\mathbf{D}}\end{bmatrix}, \bar{\mathbf{D}} = \begin{bmatrix}1 & \nu & 0\\ \nu & 1 & 0\\ 0 & 0 & \frac{1-\nu}{2}\end{bmatrix} \tag{3}$$

The elastic modulus, Poisson's ratio, and the thickness of the shell element are expressed as E, ν, and h, respectively. Matrices **B** and **D** are used to calculate the element stiffness matrix of a single shell layer. When the coordinates in the thickness direction are expressed as z, the element stiffness matrix of a single shell layer is obtained using the Jacobian matrix, **J**.

$$\mathbf{K_o} = \int_{\mathrm{v}} \mathbf{B}^{\mathrm{T}}\mathbf{D}\mathbf{B}d\mathrm{v} = \int_{-1}^{1}\int_{-1}^{1}\int_{-1}^{1} \mathbf{B}^{\mathrm{T}}\mathbf{D}\mathbf{B}\,|\mathbf{J}|\,d\xi d\eta dz \tag{4}$$

In the case of the element stiffness matrix of a composite shell layer, the element stiffness matrix is different for each shell layer and is not continuous in the z-direction. These discontinuities can be calculated by dividing and converting integral section z into z_l [42]. Here, z_l represents the coordinates of the section where the lth shell layer of the composite shell is located. The coordinate transformation is applied as follows.

$$z = -1 + [h_l(z_l - 1) + 2\sum_{i=1}^{l} h_i]/h_t, dz = dz_l h_l/h_t \tag{5}$$

Here, h_l represents the thickness of the lth shell layer, and h_t represents the total thickness of the composite shell layer element. Using the coordinate transformation, the element stiffness matrix of the composite shell layer comprising L layers is calculated.

$$\mathbf{K_{o,c}} = \sum_{l=1}^{\mathrm{L}}\int_{-1}^{1}\int_{-1}^{1}\int_{-1}^{1} \mathbf{B}_l^{\mathrm{T}}\mathbf{D}_l\mathbf{B}_l(h_l/h_t)\,|\mathbf{J}|\,d\xi d\eta dz_l \tag{6}$$

The deformation vector, **d**, represents the deformation of the structure, and is calculated using the applied load, **F**, as follows.

$$\mathbf{d} = (\mathbf{K_{o,c}})^{-1}\mathbf{F} \tag{7}$$

The deformation vector, **d**, is used to calculate the stress formed in the structure of interest. The stress values at individual integration points are given as follows.

$$\boldsymbol{\sigma} = \mathbf{DBd} \tag{8}$$

The single-shell element geometric stiffness matrix, $\mathbf{K}_{\boldsymbol{\sigma}}$, and composite shell element geometric stiffness matrix, $\mathbf{K}_{\boldsymbol{\sigma},\mathbf{c}}$, are calculated using **G** and **S**. The matrix of the shape function derivatives at each integration point and the matrix of the current Cauchy stresses are denoted by **G** and **S**, respectively.

$$\mathbf{K}_{\boldsymbol{\sigma}} = \int_{\mathrm{v}} \mathbf{G}^{\mathrm{T}}\mathbf{S}\mathbf{G}d\mathrm{v} = \int_{-1}^{1}\int_{-1}^{1}\int_{-1}^{1} \mathbf{G}^{\mathrm{T}}\mathbf{S}\mathbf{G}\,|\mathbf{J}|\,d\xi d\eta dz \tag{9}$$

$$\mathbf{K}_{\boldsymbol{\sigma},\mathbf{c}} = \sum_{l=1}^{\mathrm{L}}\int_{-1}^{1}\int_{-1}^{1}\int_{-1}^{1} \mathbf{G}_l^{\mathrm{T}}\mathbf{S}_l\mathbf{G}_l\,|\mathbf{J}|\,(h_l/h_t)d\xi d\eta dz_l \tag{10}$$

The calculated matrices can be used to formulate the eigen-buckling equation for shell element due to the thermal load.

$$[\mathbf{K_{o,c}} + \lambda_{cr}\mathbf{K}_{\boldsymbol{\sigma},\mathbf{c}}]\mathbf{v} = \mathbf{0} \tag{11}$$

The eigenvalue, λ_{cr}, is a load multiplier adjusting the thermal load vector to the critical threshold value, which induces buckling. The eigenvector, **v**, represents the shape of the buckling mode.

2.2. Optimization formulation

The optimization schemes are presented in this study. The first optimization method is the topography optimization method, setting the positions of the nodes as the design variables to optimize the structure with desired buckling temperatures. Desired temperature values can be obtained by formulating the objective function to minimize the differences of resultant and target temperature values [39]. Thus the proposed optimization formula aims to minimize the difference of the resultant and target buckling temperatures. The objective function and the bound constraints are set as follows.

$$\begin{aligned}&\mathrm{OP1}: \mathrm{Min}_{u_i} f_{obj} = \sum_{k=1}^{n}(T_{critical,k} - T_{objective,k})^2\\ &u_{\min} \le u_i \le u_{\max},\ i = 1, 2, \ldots, \mathrm{N\,nodes}\end{aligned} \tag{12}$$

The computed and target buckling temperatures of the kth buckling mode are expressed as $T_{critical,k}$ and $T_{objective,k}$, respectively. The design variables, u_i, are the offset displacement value of the ith node of the structure. The upper and lower limits of the design variable, u_i, are u_{max} and u_{min}, respectively. The number of buckling temperature values considered herein is n. The number of the nodes is N.

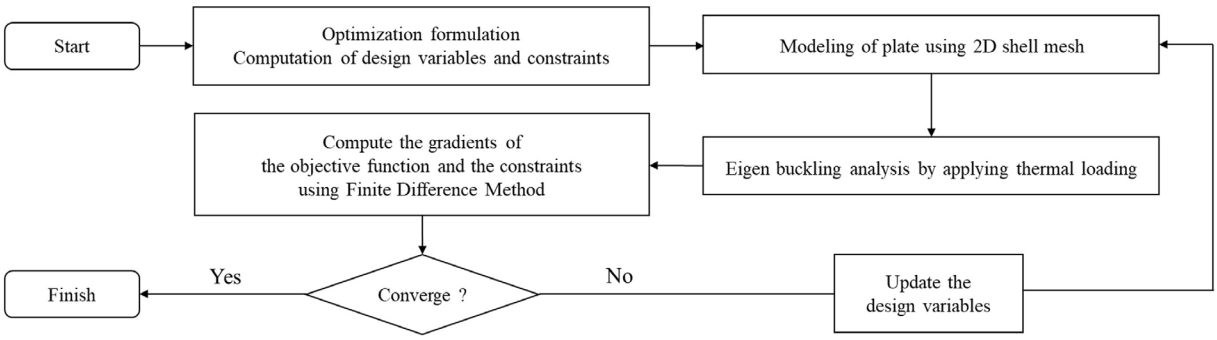

Fig. 3. Illustration of the optimization process.

The second optimization method sets the thicknesses of the shell elements as the design variables and the objective function is set as follows.

$$\begin{aligned} \text{OP2}: &\text{Min}_{t_i} f_{obj} = \sum_{k=1}^{n} (T_{critical,k} - T_{objective,k})^2 \\ &V_o \le V^* \\ &t_{\min} \le t_i \le t_{\max},\ i = 1, 2, \ldots, \text{N nodes} \end{aligned} \tag{13}$$

The design variables, t_i, are the thickness values of shell element at the ith node of the structure. The upper and lower limits of the design variable, t_i, are t_{max} and t_{min}, respectively. Unlike the topography optimization, size optimization involves changing the thickness values, resulting in a change in the total volume of the structure. Thus, volume constraint is added to the optimization formulation. The volume of the tentative structure is V_0, and the upper limit of the structure volume is V^*.

This study also aims to conduct the topography and size optimization to acquire the desired thermal buckling mode shapes. Desired geometries can be obtained by formulating the objective function to minimize the displacement difference of resultant and target geometries. Thus the proposed optimization formulation aims to minimize the displacement differences of the resultant and target buckling mode shapes. The optimization formulations of the two methods for controlling the buckling mode shapes are set as follows.

$$\begin{aligned} \text{OP3}: &\text{Min}_{u_i} f_{obj} = \sum_{k=1}^{n} (\delta_{critical,k} - \delta_{objective,k})^2 \\ &u_{\min} \le u_i \le u_{\max},\ i = 1, 2, \ldots, \text{N nodes} \end{aligned} \tag{14}$$

$$\begin{aligned} \text{OP4}: &\text{Min}_{t_i} f_{obj} = \sum_{k=1}^{n} (\delta_{critical,k} - \delta_{objective,k})^2 \\ &V_o \le V^* \\ &t_{\min} \le t_i \le t_{\max},\ i = 1, 2, \ldots, \text{N nodes} \end{aligned} \tag{15}$$

The displacement values of the kth buckling mode shape and the target buckling mode shape from the initial structural geometry are expressed as $\delta_{critical,k}$ and $\delta_{objective,k}$, respectively. The design variables and constraints in Eqs. (14) and (15) are identical to those of Eqs. (12) and (13), respectively.

The buckling-related sensitivity analysis based on the finite difference method (FDM) is employed after formulating the above optimization formulations. The buckling analysis is performed by applying thermal load to composite structure. The buckling temperature can be obtained by multiplying the eigenvalue obtained through the analysis with the thermal load value. The optimization process proceeds until the target buckling temperature or the target mode shape is achieved as shown in Fig. 3.

3. Optimization results

This section presents several optimization examples to validate the present optimization formulations. The MATLAB optimizer, fmincon, is used to solve the optimization problems in the integrated framework of ANSYS APDL. The optimization examples are carried out on the composite structures of 100 mm × 10 mm or 100 mm × 100 mm, as shown in Fig. 4(a). The ends of the structures are clamped. The two structures are modeled using four-node shell 181, with initial shell thickness values of 1.5 mm. To validate the FEM for the considered buckling problems, analysis is done on composite structures of 100 mm × 10 mm comprising different numbers of elements. Note that the number of elements in the length direction are equal to that in the width direction. Fig. 4(b) shows the results of the first, second, and third buckling temperatures. From the results, the buckling temperatures converge when the structures comprise more than 25 elements, indicating that the FEM is valid for buckling analysis of those structures. Based on the results, the composite structures used for the optimization examples are modeled with 25 elements and 36 nodes.

3.1. Sensitivity analysis

The present structural optimization scheme considers the node position (topography optimization) or element thickness (size optimization) at each node as the design variable. Because the two composite structures shown in Fig. 4 are modeled with 36 nodes, 36 design variables are optimized in the case studies. The sensitivity of the objective function can be calculated efficiently using the FDM. To prove this, sensitivity analysis is carried out on a 100 mm × 10 mm plate. The design variables are set as the thicknesses of the elements at each node. The left and right ends of the structure, which are based on Fig. 5(a), are clamped, and the FDM sensitivity analysis is conducted by applying temperature load to the entire surface. Fig. 5(b) shows the results of the sensitivity analysis with respect to the perturbed design values. As the ends of the structure are constrained and the temperature load is applied to the entire surface, the sensitivity values are symmetric vertically and horizontally. Fig. 5(b) shows that the eight chosen design parameters, which are specified in Fig. 5(a), have the same sensitivity values for each symmetric position, regardless of the perturbation values. Based on the results of the sensitivity analysis, the optimization processes can be carried out, with the perturbation values of the design variables set as 0.01 mm for all cases.

3.2. Topography optimization: Control of buckling temperature

The first optimization example is to control the buckling temperature of the first three modes using the topography optimization method. The design variables in this optimization scheme are the positions of the 36 nodes. The optimal design is applied on a 100 mm × 10 mm plate. The thickness of the structure is set as 1.5 mm. Linear eigenbuckling analysis is conducted by applying temperature load to the elements of the structure. Two case studies are considered in this example, the first case that has the temperature load applied to the entire structure surface, and the second case that has the temperature load applied to only certain parts of the structure surface. Fig. 6(a)

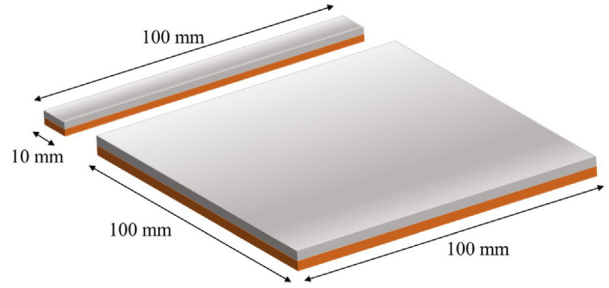

Material properties	Top steel layer	Bottom copper layer
Young's Modulus	200 GPa	128 GPa
Poisson's ratio	0.30	0.36
Thermal expansion coefficient	11.7×10^{-6} °C^{-1}	17.0×10^{-6} °C^{-1}

(a)

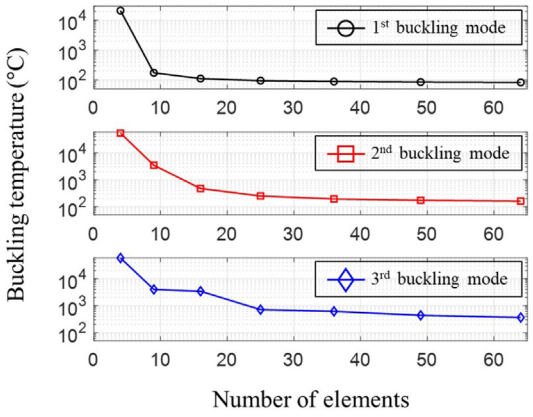

(b)

Fig. 4. (a) Composite structures used for examples and (b) buckling temperature values of structures with different element numbers.

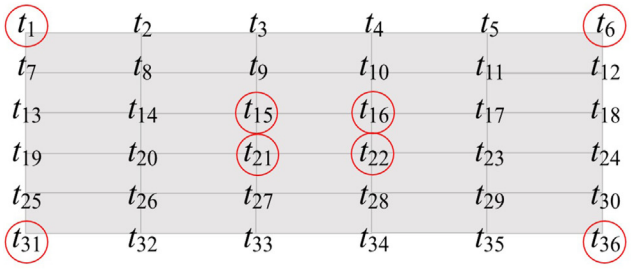

(a)

Design Variable	Sensitivity when $\Delta t = 0.1$ mm	Sensitivity when $\Delta t = 0.01$ mm	Sensitivity when $\Delta t = 0.001$ mm
t_1	0.9070 °C/mm	0.8900 °C/mm	0.8800 °C/mm
t_6	0.9070 °C/mm	0.8900 °C/mm	0.8800 °C/mm
t_{15}	2.8380 °C/mm	2.7800 °C/mm	2.7000 °C/mm
t_{16}	2.8380 °C/mm	2.7800 °C/mm	2.7000 °C/mm
t_{21}	2.8380 °C/mm	2.7800 °C/mm	2.7000 °C/mm
t_{22}	2.8380 °C/mm	2.7800 °C/mm	2.7000 °C/mm
t_{31}	0.9070 °C/mm	0.8900 °C/mm	0.8800 °C/mm
t_{36}	0.9070 °C/mm	0.8900 °C/mm	0.8800 °C/mm

(b)

Fig. 5. Sensitivity analysis: (a) Design variables and (b) FDM test results.

shows an illustration of the heated elements of the structure for the first case, where the elements shaded in red have temperature loading applied. In the first case study, the initial buckling temperatures of the structure are 94.9640 °C, 249.5486 °C, and 710.2855 °C for the first three buckling modes. The optimization aims to increase the buckling temperature. The target buckling temperature values are increased by approximately 20 °C, 40 °C, and 60 °C from the initial buckling temperature values. Thus, the target buckling temperature values for the first case are set as 115 °C, 290 °C, and 770 °C for the first three buckling modes. The upper and lower limits of the node displacement are set as 5.00 and −5.00 mm from the initial positions, respectively. The displacement values of each node are obtained by applying the optimization and shown in Fig. 6(b).

It can be observed from the optimization result that the positions of the nodes at the edges and center of the structure show small changes, with displacement values of the nodes having values of between 0.0000 and 1.0000 mm in the out-of-plane direction. The remaining nodes show greater offset displacement values ranging between 2.8731 and 5.0000 mm in the out-of-plane direction. Because the example is symmetric, the optimized structure also shows a symmetric result in both the vertical and horizontal directions, where both ends of the plate are clamped, and temperature load is applied to the entire surface. The resultant first, second, and third buckling temperatures of the optimized structure are changed to 115.6351 °C, 287.3625 °C, and 772.7367 °C, respectively. The resultant buckling temperatures are close to the target buckling temperatures, with errors of 0.5523%, 0.9095%, and 0.3554% for the first three buckling modes.

In the second case, the temperature load in Fig. 7(a) is applied to certain parts of the structures. In this case, the initial buckling temperatures of the structure are 72.5129 °C, 124.6304 °C, and 454.4162 °C for the first three buckling modes. The optimization aims to increase the buckling temperature. As in the first case, the target buckling temperatures are increased by approximately 20 °C, 40 °C, and 60 °C from the initial buckling temperatures. Thus the target buckling temperatures for the second case are set as 95 °C, 165 °C, and 515 °C for the first three buckling modes. The upper and lower limits of the node displacement are set as 5.00 mm and −5.00 mm from the initial positions, respectively. The displacement values of each node are obtained by conducting the optimization, and the results are shown in Fig. 7(b).

It can be observed that the results show significant differences with the results of the first case study. Unlike the first case study, the resultant displacements of the nodes do not show the symmetric tendency, and negative displacements can be observed in the results. The resultant first, second, and third buckling temperatures of the optimized structure are changed to 94.6155 °C, 165.0251 °C, and 515.2912 °C, respectively. The resultant buckling temperatures are close to the target buckling temperature with errors of 0.4047%, 0.0152%, and 0.0565%, respectively, for the first three buckling modes. The results of the topography optimization to control buckling temperature are shown in Fig. 8. The errors for all cases are below 1%, indicating that the topography optimization allows the convergence of the first, second, and third buckling temperatures to the target values successfully. Among the two cases, the asymmetric temperature load case converges closer to the target values, where error rates are lower than those of the symmetric temperature load case for all three buckling modes. Overall, the case studies show that the present method is applicable for both symmetric and asymmetric load conditions.

3.3. Size optimization: Control of buckling temperature

The next example is conducted to control the buckling temperature in the framework of size optimization. Similar to the previous example, two case studies are conducted in this example. The design variables in

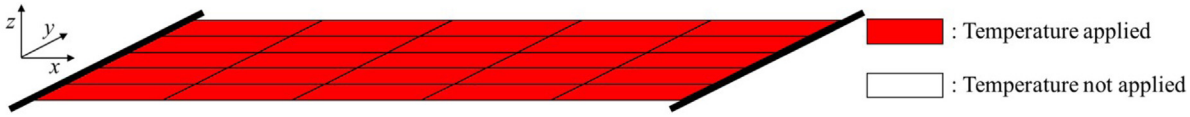

(a)

Node displacement from initial position in mm

0.0000	0.9500	0.7605	0.7605	0.9500	0.0000
0.0000	2.8731	4.0775	4.0775	2.8731	0.0000
0.0000	5.0000	0.0000	0.0000	5.0000	0.0000
0.0000	5.0000	0.0000	0.0000	5.0000	0.0000
0.0000	2.8731	4.0775	4.0775	2.8731	0.0000
0.0000	0.9500	0.7605	0.7605	0.9500	0.0000

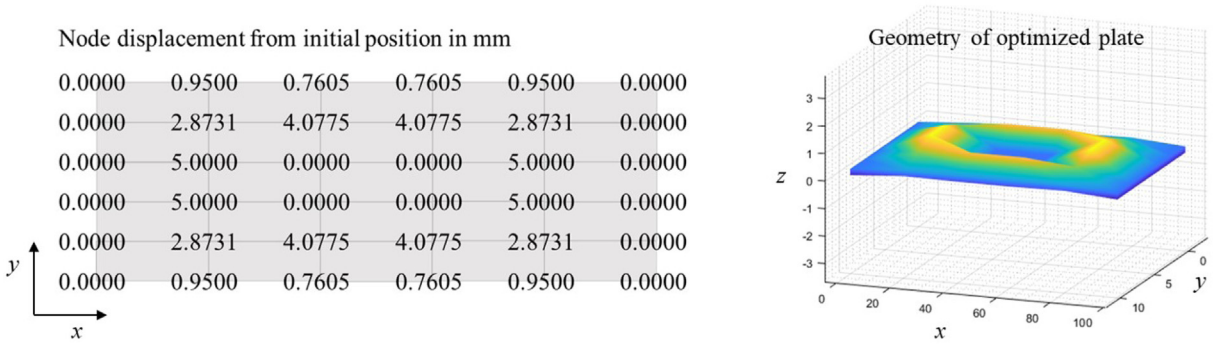

(b)

Fig. 6. Illustration of topography optimization: (a) Temperature load application and (b) optimized plate.

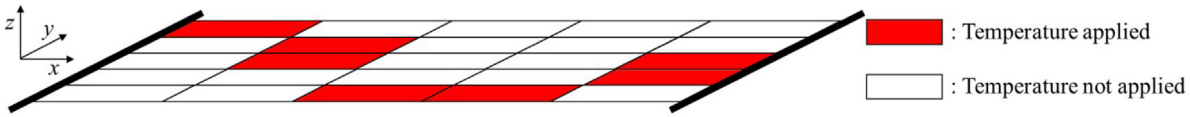

(a)

Node displacement from initial position in mm

0.0000	-3.3050	1.4021	-1.2424	-3.5095	0.0000
0.0000	1.8393	-0.5122	0.7569	0.6553	0.0000
0.0000	0.8268	-3.6068	-0.2361	0.0987	0.0000
0.0000	0.1460	0.0431	0.9090	0.3094	0.0000
0.0000	0.9116	0.8821	-0.0115	1.4179	0.0000
0.0000	0.5504	-0.1839	-0.1477	0.4758	0.0000

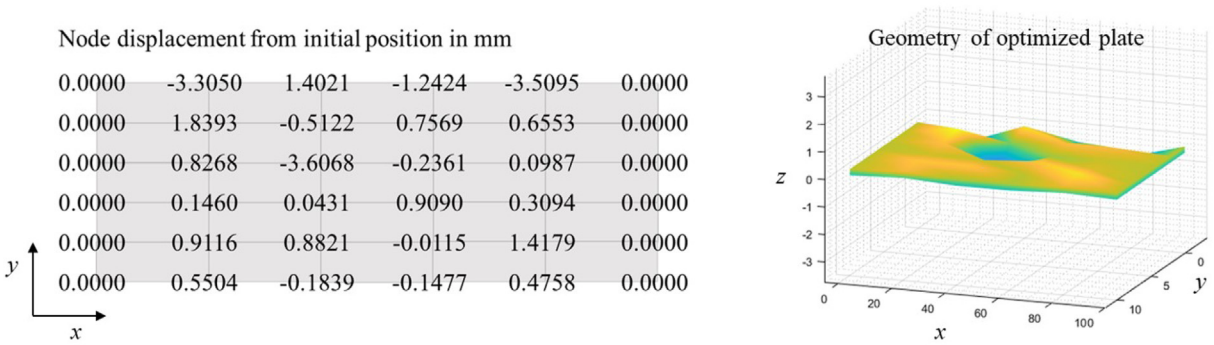

(b)

Fig. 7. Illustration of topography optimization: (a) Temperature load application and (b) optimized plate.

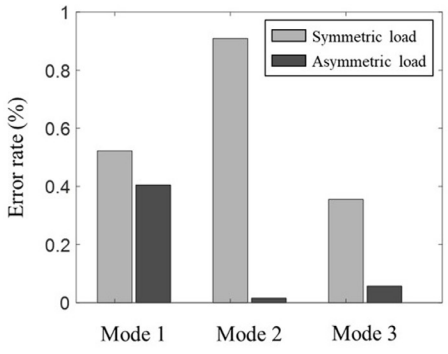

	Temperature load symmetric distribution			Temperature load asymmetric distribution		
	Target temperature	Resultant temperature	Error*	Target temperature	Resultant temperature	Error*
1st mode	115.0000 °C	115.6351 °C	0.5523%	95.0000 °C	94.6155 °C	0.4047%
2nd mode	290.0000 °C	287.3625 °C	0.9095%	165.0000 °C	165.0251 °C	0.0152%
3rd mode	770.0000 °C	772.7367 °C	0.3554%	515.0000 °C	515.2912 °C	0.0565%

$$* \text{Error} = \frac{|\text{Resultant temperature} - \text{Target temperature}|}{\text{Target temperature}} \times 100\%$$

Fig. 8. Summarized results of topography optimization to control buckling temperature.

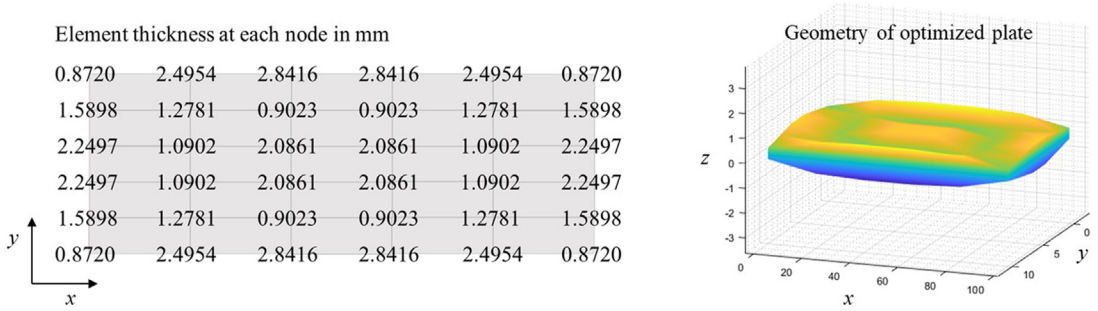

Fig. 9. Illustration of optimized plate after size optimization.

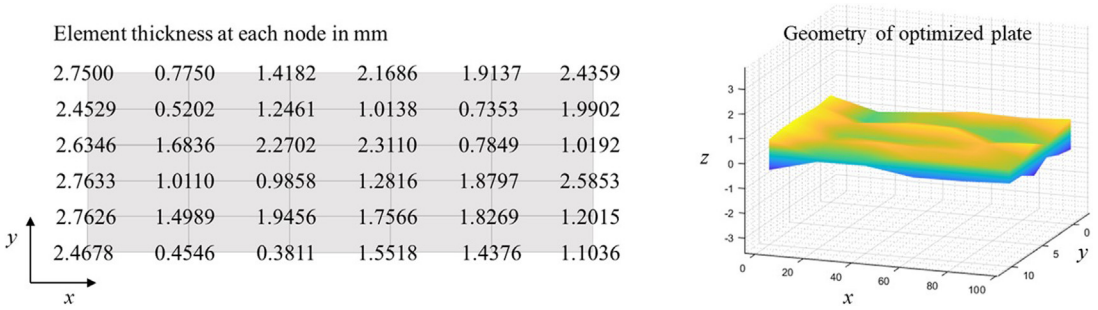

Fig. 10. Illustration of optimized plate after size optimization.

this optimization scheme are the thickness values of the shell elements at the 36 nodes. The optimization domain is set as a 100 mm × 10 mm composite plate shown in Fig. 4. The initial thickness of the structure is set as 1.5 mm. Linear eigen-buckling analysis is conducted by applying temperature load to the elements of the structure. The elements applied with temperature load are identical to those of the previous example, where temperature load is applied to the entire structure surface in the first case and to certain parts of the structure surface in the second case as shown in Figs. 6(a) and 7(a). The initial conditions of the optimization procedure are identical to those used in the previous example. Consequently, the initial buckling temperature values of the structure are identical to those of the first example for both case studies. The target buckling temperature values are also established identically. The upper and lower limits of the element thickness are set as 3.00 mm and 0.30 mm, respectively. The thickness values of the elements at each node are obtained by applying the size optimization. The result for the first case is presented in Fig. 9.

For the first case, except for the four corners of the structure, the thickness of the elements at the edges and center of the structure generally become thicker, with the thicknesses of the shell elements ranging between 1.5898 mm and 2.8416 mm. The remaining elements, positioned at the four corners and between the edges and the center of the structure, show decrease in thicknesses, ranging between 0.8720 mm and 1.2781 mm. Identical to the first topography optimization case study, the results of this size optimization case study show a symmetric trend in both the vertical and horizontal directions. The symmetric boundary and loading condition resulted in the symmetric thickness distribution. The resultant first, second, and third buckling temperatures of the optimized structure are changed to 114.1030 °C, 291.7120 °C, and 764.5235 °C, respectively. The resultant buckling temperatures are close to the target temperature, with error values of 0.7800%, 0.5903%, and 0.7112%.

The results for the second case are presented in Fig. 10. In this case, the results do not show a symmetric trend, due to the asymmetric loading condition. The resultant buckling temperatures of the optimized structure are changed to 95.0175 °C, 164.9842 °C, and 512.8700 °C for the first three buckling modes. Again, the resultant buckling temperature values are close to the target temperature with errors of 0.0184%, 0.0096%, and 0.4136%, respectively, for the first three buckling modes. The results of the size optimization to control buckling temperature are shown in Fig. 11. Like the topography optimization method, the errors for all cases are below 1%, indicating that the size optimization using the element thickness allows the convergence of the first, second, and third buckling temperatures of the composite structure to the target values for both symmetric and asymmetric cases. Among the two cases, the asymmetric temperature load case converges closer to the target values, with lower error rates than those of the symmetric temperature load case for all three buckling modes. Overall, the case studies show that the size optimization method is applicable for both symmetric and asymmetric load conditions.

3.4. Topography optimization: Control of buckling mode shape

Previous examples show that both topography and size optimization methods can be used to control the buckling temperature values by changing the node positions or element thicknesses. The following examples are conducted to show that buckling mode shapes can be controlled using the proposed structural optimization methods. In this example, topography optimization is used to change the first buckling mode shape to the desired geometry. The design variables are the positions of the 36 nodes. Unlike the previous buckling temperature examples, the optimal design is applied on a 100 mm × 100 mm plate in this example, because the deformation value is too small for analysis when using a 100 mm × 10 mm plate. The thickness of the structure is set as 1.5 mm. Linear eigen-buckling analysis is conducted by applying temperature load to all elements of the structure. The first buckling mode of the structure occurs at 92.7467 °C, and the initial first buckling mode shape is as shown in Fig. 12.

The target buckling mode shape is set to have the center of the structure bulge up, whereas the rest of the parts have minimum deformation. This is achieved by maximizing the deformation value of the four nodes at the center, and by setting the deformation of the remaining nodes to zero in the formulation of the objective function. The upper and lower limits of the node displacement are set as 5.00 and −5.00 mm from the initial positions, respectively. The displacement of each node is obtained by conducting the optimization scheme; the

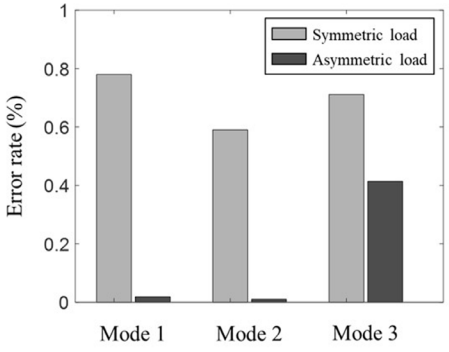

	Temperature load symmetric distribution			Temperature load asymmetric distribution		
	Target temperature	Resultant temperature	Error*	Target temperature	Resultant temperature	Error*
1st mode	115.0000 °C	114.1030 °C	0.7800%	95.0000 °C	95.0175 °C	0.0184%
2nd mode	290.0000 °C	291.7120 °C	0.5903%	165.0000 °C	164.9842 °C	0.0096%
3rd mode	770.0000 °C	764.5235 °C	0.7112%	515.0000 °C	515.8700 °C	0.4136%

$$* \text{Error} = \frac{|\text{Resultant temperature} - \text{Target temperature}|}{\text{Target temperature}} \times 100\%$$

Fig. 11. Summarized results of size optimization to control buckling temperature.

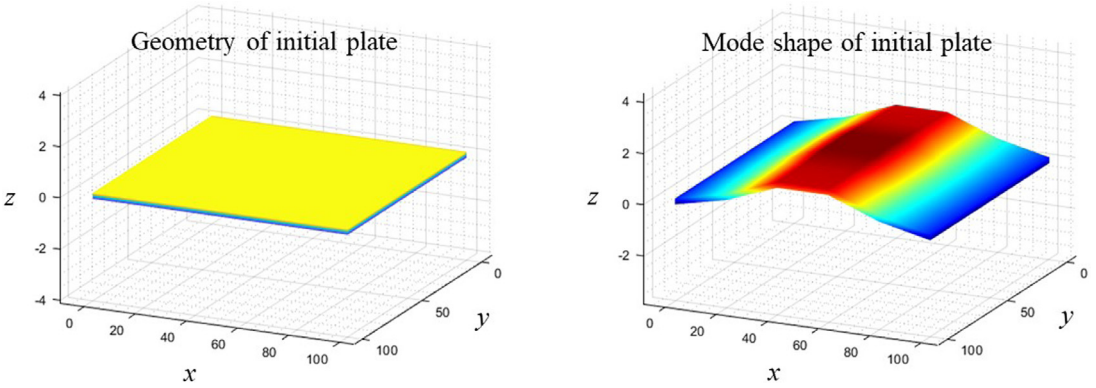

Fig. 12. Initial plate geometry and mode shape.

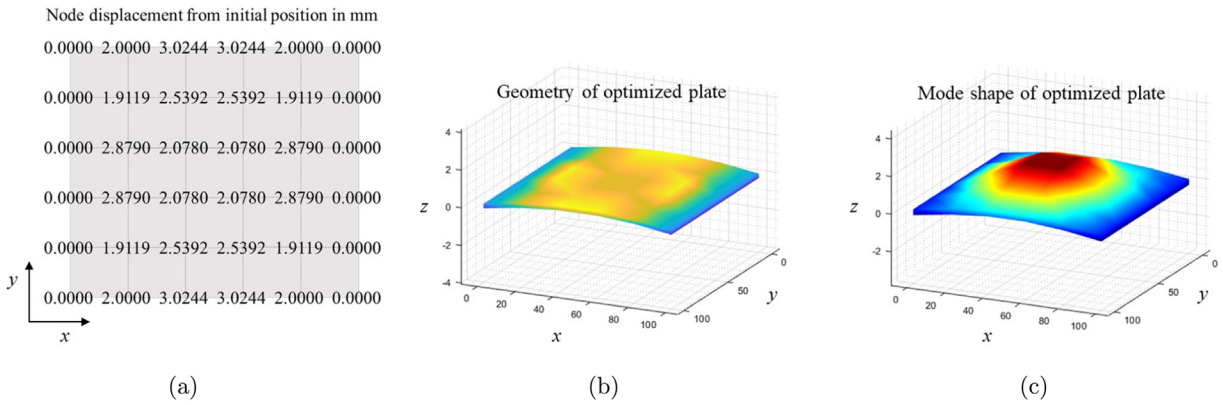

Fig. 13. Optimization results: (a) Node position, (b) plate geometry, and (c) mode shape.

results are shown in Fig. 13(a). The positions of the nodes do not show any negative values, wherein the displacement values of the nodes are between 0.0000 and 3.0224 mm in the out-of-plane direction. The changes in the node positions make the initially flat plate have a natural arch-shaped geometry, with the center of the plate slightly submerged. The geometry of the composite plate and the associated first buckling mode shapes are illustrated in Fig. 13(b) and (c). Although the first buckling mode shape cannot be numerically compared with the target mode shape, it is evident that the mode shape resembles a volcano visually, with only the center of the plate bulging up as desired. From this example, it can be seen that the proposed topography optimization method can change the buckling mode shape to the desired geometry.

3.5. Size optimization: Control of buckling mode shape

This optimization example is conducted to control the first buckling mode shape using size optimization. The design variables are the thicknesses of the shell elements at the 36 nodes. The optimal design is applied on a 100 mm × 100 mm plate. The initial thickness of the structure is set as 1.5 mm. Linear eigen-buckling analysis is conducted by applying temperature load to all elements of the structure. The initial conditions of the optimization procedure are identical to those of the previous buckling mode shape example. Consequently, the initial first buckling temperature and buckling mode shape of the structure are identical to those of the previous example, as indicated in Fig. 12. The target buckling mode shape is also identical to the previous buckling mode shape example, where the target buckling mode shape is set to have the center of the structure bulge up, with the remainder having

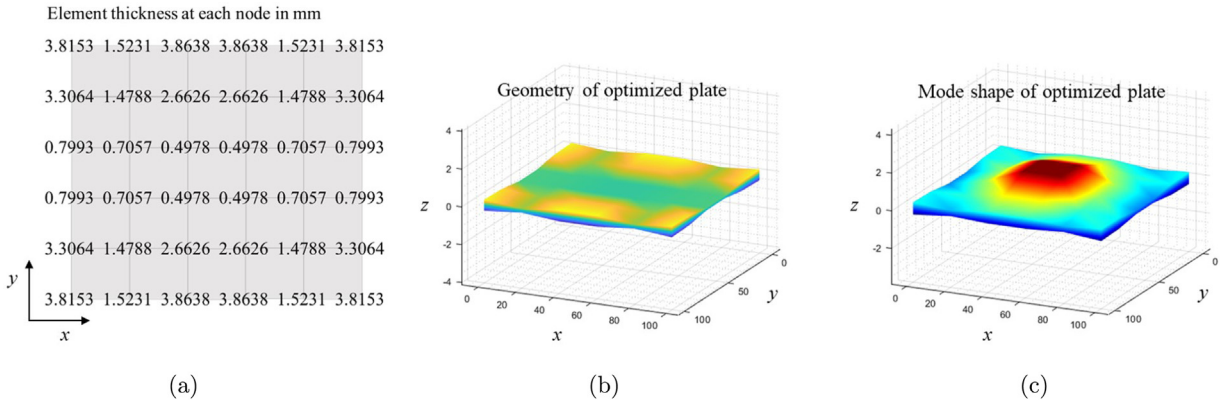

Fig. 14. Optimization results: (a) Node thickness, (b) plate geometry, and (c) mode shape.

minimum deformation. An identical procedure is conducted in the formulation of the objective function. The upper and lower limits of the element thickness are set as 5.00 mm and 0.30 mm, respectively. The thicknesses of the elements at each node are obtained by performing the optimization, the results of which are shown in Fig. 14(a). The results show that the upper and lower sections of the structure generally become thicker, whereas the center section of the structure decreases in thickness, ranging between 0.4978 and 0.7993 mm. The geometry of the composite plate and the associated first buckling mode shapes are illustrated in Fig. 14(b) and (c). Although the first buckling mode shape cannot be numerically compared with the target mode shape, it is apparent that the mode shape resembles a volcano visually with only the center of the plate bulging up as desired. Similar to the topography optimization method, the size optimization method makes it possible to change the geometry of the first buckling mode shape to the desired geometry, thus showing that the proposed optimization frameworks are capable of controlling the buckling mode shapes.

3.6. Optimization considering the centrifugal force

For the last engineering application, the present optimization scheme is now applied in order to control the thermal buckling temperature and the buckling mode shapes considering the centrifugal effect. The centrifugal force is formulated in the eigen-buckling analysis using the following formulation.

$$\mathbf{F} = \mathbf{F}_T + \mathbf{F}_C, \quad \mathbf{F}_C = m\boldsymbol{\omega} \times (\boldsymbol{\omega} \times \boldsymbol{r}) \tag{16}$$

Note that the centrifugal force is dependent on the design variables. The centrifugal force $\mathbf{F}_C$ is added to the temperature load $\mathbf{F}_T$ to form the total applied load $\mathbf{F}$. The centrifugal force is calculated using the mass, angular velocity and distance of the object from the rotating axis, each denoted by m, $\boldsymbol{\omega}$ and $\boldsymbol{r}$ respectively.

To verify the effects of centrifugal force, the present example considers a rotating steam turbine blade. The diameter, length and maximum width of the blade are set as 1200 mm, 1000 mm and 500 mm, respectively. The maximum thickness is set as 52.5 mm and it is assumed that the thickness values of the cross-section of the blade are constant in the length direction. The turbine rotor is designed to have diameter of 1200 mm. The material properties of steel are assigned for the finite element turbine blade model. The model is discretized by 400 four-node shell elements of ANSYS (Element 181) for accurate and valid buckling analysis. The boundary conditions are imposed along the bottom section of the blade and the eigen-buckling analysis is carried out by applying temperature load to all elements and by rotating the blade (the centrifugal force). The geometry, temperature load dissipation and the initial thickness distributions of the blade are summarized in Fig. 15(a) and (b).

To observe the influence of centrifugal force before the optimization, the blade is rotated and the eigen-buckling analysis with the centrifugal force is carried out. The first three buckling temperatures of a stationary turbine blade with the initial thickness values are 287.5912 °C, 318.1598 °C, and 548.7110 °C, respectively. By increasing the angular velocity of the blade and increasing the magnitudes of the centrifugal force, the buckling temperatures and the buckling modes are subject to be changed accordingly. Fig. 16 illustrates the curves of the three buckling temperatures with respect to the rotating speed of the blade. It is observed that the buckling temperature values decrease and the first and the second buckling temperatures merge after 50 rad/s approximately. Not only the buckling temperatures, but also the buckling modes are influenced due to the centrifugal force. Thus, it is challenging to consider the effect of this angular velocity during an optimization process.

In this example, we aim to increase the buckling temperature with and without the centrifugal force. With zero rotational speed (no centrifugal force), the target buckling temperatures are set as 320 °C, 360 °C, and 600 °C. For the rotation case with angular velocity of 50 rad/s, the target temperatures are set as 135 °C, 150 °C, and 225 °C. These values are chosen to increase the first three buckling temperatures by 30 °C, 40 °C and 50 °C respectively, and are arbitrary chosen to set the first three buckling temperatures differently. The thickness values can be varied between −2mm and 2 mm from the initial thickness values considering the airfoil geometry. Note that the thickness values of the elements are constant along the blade direction. The optimization results are summarized in Figs. 17 and 18.

The optimized thicknesses without the consideration of blade rotation are presented in Fig. 18(a). The 12 design variables are increased and the 9 design variables are decreased among the 21 nodal thickness values resulting the volume increase about 0.4132%. After the optimization, the buckling temperatures are changed to 324.1225 °C, 365.8901 °C, and 592.2094 °C. The resultant buckling temperatures are close to the target temperatures, with error values of 1.2883%, 1.6361%, and 1.2984%, respectively. Considering the rotation of the blade and the centrifugal force, the optimization result with the increased 17 design values and the decreased 4 design variables is obtained in Fig. 18(b). After the optimization process, the volume is increased about 4.2067% and the first three buckling temperatures are changed to 138.8979 °C, 146.0847 °C, and 227.9672 °C. The resultant buckling temperatures are close to the target temperatures, with error values of 2.8873%, 3.2769%, and 1.3188%, respectively. This example shows that the rotation plays an important role in the determination of buckling temperature and the present optimization scheme can successfully consider the effect of rotation and the centrifugal force on the buckling temperature. From an engineering point of view, thus, it is important to consider the effect of the centrifugal force not only for the static failure but also the dynamic failure.

The next example aims to control the buckling mode shape of the turbine blade. The eigen-buckling analysis of the initial model of the turbine blade is conducted to determine the first buckling mode. As

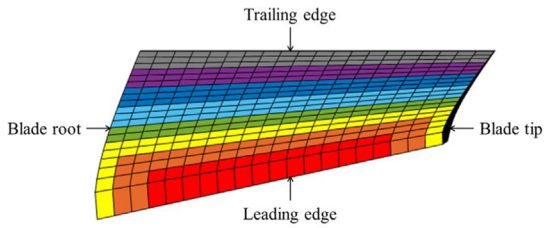

Color of element	Temperature load
Red	1.0000°C
Orange	0.9300°C
Yellow	0.8600°C
Green	0.7900°C

Color of element	Temperature load
Light blue	0.7200°C
Navy	0.6500°C
Purple	0.5800°C
Grey	0.5000°C

(a)

Turbine blade's cross-section

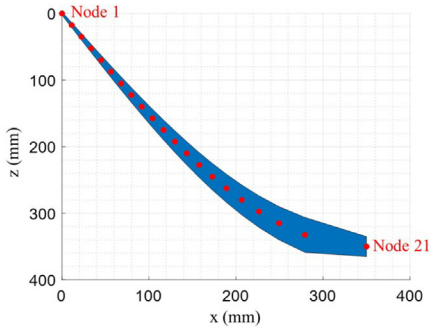

Initial thickness of turbine blade nodes

Node number	Thickness values
1	5.0000 mm
2	7.5000 mm
3	10.0000 mm
4	12.5000 mm
5	15.0000 mm
6	17.5000 mm
7	20.0000 mm

Node number	Thickness values
8	22.5000 mm
9	25.0000 mm
10	27.5000 mm
11	30.0000 mm
12	32.5000 mm
13	35.0000 mm
14	37.5000 mm

Node number	Thickness values
15	40.0000 mm
16	42.5000 mm
17	45.0000 mm
18	47.5000 mm
19	50.0000 mm
20	52.5000 mm
21	30.0000 mm

(b)

Fig. 15. (a) Temperature load on turbine blade and (b) initial element thickness values at each node of the turbine blade.

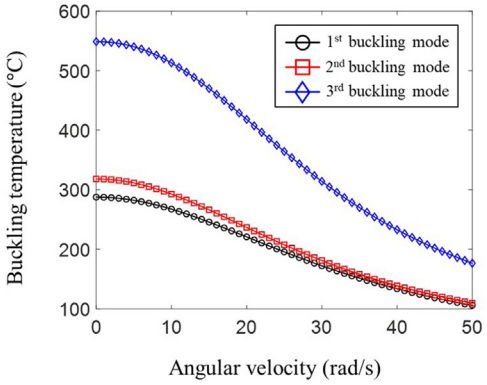

Buckling temperature with zero angular velocity

1st buckling mode temperature (°C)	2nd buckling mode tem perature (°C)	3rd buckling mode temperature (°C)
287.5912	318.1598	548.7110

Buckling temperature with 50 rad/s angular velocity

1st buckling mode temperature (°C)	2nd buckling mode tem perature (°C)	3rd buckling mode temperature (°C)
105.9395	109.5433	176.5182

Fig. 16. Buckling temperatures of the buckling modes at different angular velocities.

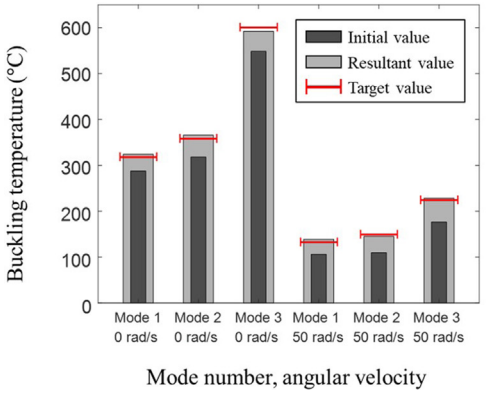

Buckling temperature with zero angular velocity

1st buckling mode temperature (°C)	2nd buckling mode tem perature (°C)	3rd buckling mode temperature (°C)
287.5912→324.1226	318.1598→365.8901	548.7110→592.2094

Buckling temperature with 50 rad/s angular velocity

1st buckling mode temperature (°C)	2nd buckling mode tem perature (°C)	3rd buckling mode temperature (°C)
105.9395→138.8979	109.5433→145.0847	176.5182→227.9672

Fig. 17. Initial values, target values, and resultant values of buckling temperatures of first three buckling modes with angular velocity of 50 rad/s.

in the previous example, the optimization problems without and with the centrifugal force of 50 rad/s are considered. The initial shapes of the first buckling modes of the two cases are shown in Fig. 19. It is observed that some instabilities are present at the trailing edge and near

Turbine blade's cross-section

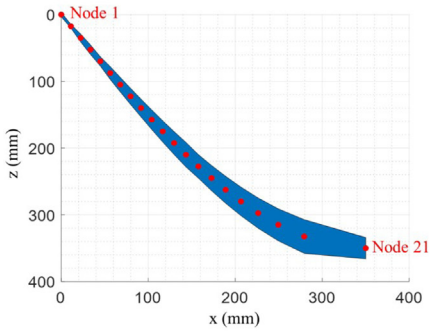

Optimized thickness of turbine blade nodes (Case without angular velocity)

Node number	Thickness values	Node number	Thickness values	Node number	Thickness values
1	7.0000 mm	8	24.5000 mm	15	38.0000 mm
2	5.6321 mm	9	27.0000 mm	16	40.5000 mm
3	12.0000 mm	10	29.5000 mm	17	43.0000 mm
4	14.5000 mm	11	32.0000 mm	18	45.5000 mm
5	14.1073 mm	12	34.5000 mm	19	48.0000 mm
6	19.5000 mm	13	37.0000 mm	20	50.5000 mm
7	22.0000 mm	14	35.5000 mm	21	32.0000 mm

(a)

Turbine blade's cross-section

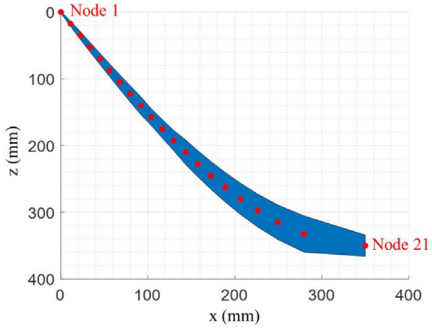

Optimized thickness of turbine blade nodes (Case with angular velocity)

Node number	Thickness values	Node number	Thickness values	Node number	Thickness values
1	3.0000 mm	8	24.5000 mm	15	42.0000 mm
2	7.9519 mm	9	27.0000 mm	16	44.5000 mm
3	12.0000 mm	10	25.5000 mm	17	47.0000 mm
4	14.5000 mm	11	28.0000 mm	18	49.5000 mm
5	17.0000 mm	12	30.5000 mm	19	52.0000 mm
6	19.5000 mm	13	37.0000 mm	20	54.5000 mm
7	22.0000 mm	14	39.5000 mm	21	32.0000 mm

(b)

Fig. 18. Optimized element thickness values at each node of turbine blade's cross-sections: (a) Static case and (b) rotating case.

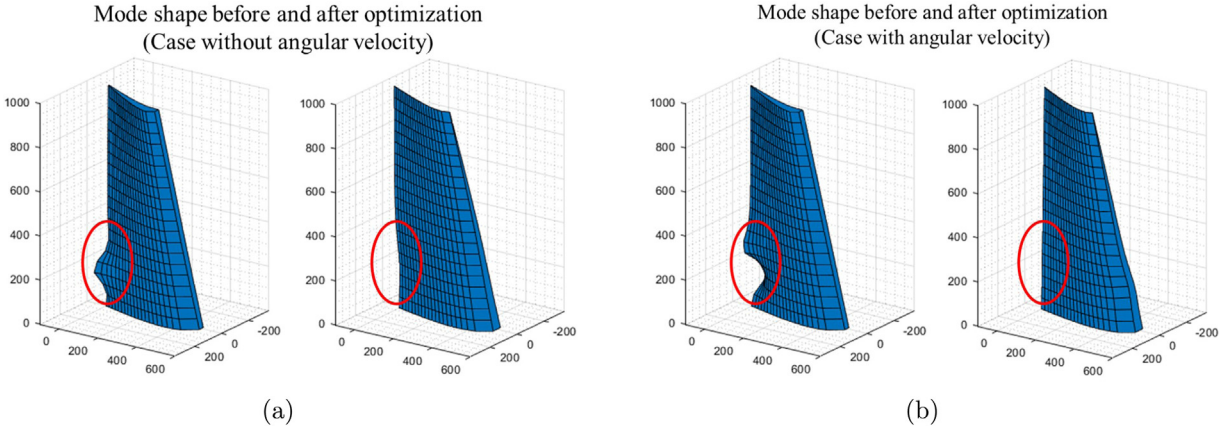

Fig. 19. First mode of turbine blade: (a) Static case and (b) rotation case.

the constrained bottom section of the blade. Thus, the optimization problem aims to increase the stability along the trailing edge. To achieve this, the optimization problem minimizing the deformation of the corresponding nodes at the trailing edge is considered. For the thickness constraints, the thickness values are set to increase linearly along the top cross-section to the bottom cross-section. The thicknesses of the top sections are set to have values of 1.00 mm. The thickness of the bottom sections are set to run values between 10.00 mm and 80.00 mm. With the present formulation, the optimization results in Figs. 19 and 20 are obtained.

The results in Fig. 20 show the thicknesses of the bottom sections of the blade. The top sections have constant thickness values of 1.00 mm, and the elements between the top and bottom sections have linearly increasing thicknesses proportionally from the top to the bottom for the both cases. The thickness values of the elements in the bottom section vary between 39.4576 mm and 53.8097 mm for the static case, and vary between 30.0000 mm and 60.0000 mm for the rotation case (50 rad/s). Fig. 19(a) and (b) show that the buckling modes for the two cases and it turns out that the local instabilities marked by the red circles are removed after the optimization processes. This example indicates that the present optimization process is effective to remove the local instability considering the centrifugal force.

The engineering application of the size optimization on the reaction turbine blade shows that the proposed optimization scheme can be used to control the buckling temperature and buckling mode shapes to achieve structural stability. Regardless of the structural complexity,

Turbine blade's bottom cross-section

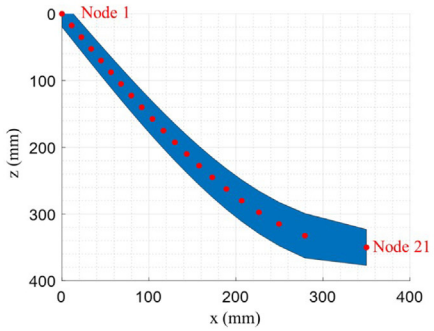

Optimized thickness of turbine blade nodes (Case without angular velocity)

Node number	Thickness values	Node number	Thickness values	Node number	Thickness values
1	39.4576 mm	8	49.5041 mm	15	59.5506 mm
2	40.8928 mm	9	50.9393 mm	16	60.9858 mm
3	42.3281 mm	10	52.3745 mm	17	62.4210 mm
4	43.7633 mm	11	53.8097 mm	18	63.8562 mm
5	45.1985 mm	12	55.2449 mm	19	65.2914 mm
6	46.6337 mm	13	56.6801 mm	20	66.7266 mm
7	48.0689 mm	14	58.1154 mm	21	53.8097 mm

(a)

Turbine blade's bottom cross-section

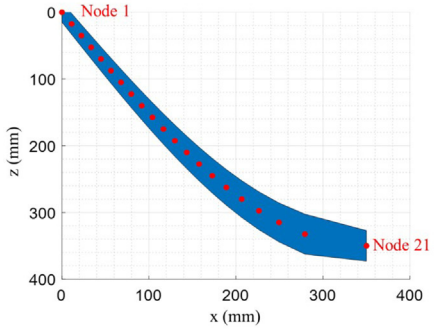

Optimized thickness of turbine blade nodes (Case with angular velocity)

Node number	Thickness values	Node number	Thickness values	Node number	Thickness values
1	30.0000 mm	8	41.0526 mm	15	52.1053 mm
2	31.5789 mm	9	42.6316 mm	16	53.6842 mm
3	33.1579 mm	10	44.2105 mm	17	55.2632 mm
4	34.7368 mm	11	45.7895 mm	18	56.8421 mm
5	36.3158 mm	12	47.3684 mm	19	58.4211 mm
6	37.8947 mm	13	48.9474 mm	20	60.0000 mm
7	39.4737 mm	14	50.5263 mm	21	45.7895 mm

(b)

Fig. 20. Optimized element thickness values at each node of turbine blade's bottom cross-sections: (a) Static case and (b) rotation case.

presence of heat dissipation within the structure, and the presence of centrifugal force, the optimization method is successful in achieving the desired buckling temperatures and buckling mode shapes. Thus, the proposed optimization method can be applied to various engineering problems, showing its capability to solve structural instabilities that are present in thermal buckling cases, while preventing an increase in the material costs.

4. Conclusion

This study proposed new optimization methods for controlling the buckling temperatures and buckling mode shapes of composite structures. Achieving structural stability by predicting and preventing unexpected buckling phenomena are critical issues in the engineering field. To overcome these issues, the buckling temperature and buckling modes were numerically analyzed using computational theories and mathematical programming. To validate the proposal, this study considered composite plates, and formulated structural optimization case studies using the node positions and element thicknesses as the design variables. The optimization formulations helped determine optimal structural designs with the desired buckling temperature values and buckling mode shapes. The proposed optimization scheme was also applied to ensure the stability of the reaction turbine blade and validate its application to practical engineering problems. Despite the structural complexity, presence of heat dissipation within the turbine blade, and the presence of centrifugal force, optimization was successful in solving the structural instabilities present in thermal buckling. In conclusion, this study proposed and validated several optimization frameworks, to control the buckling temperature and buckling mode shape of composite structures.

CRediT authorship contribution statement

Hoo Min Lee: Data collection, Data analysis and interpretation, Drafting the article. **Kang Kuk Lee:** Data collection, Data analysis and interpretation. **Gil Ho Yoon:** Conception or design of the work, Revision of the article.

Declaration of competing interest

The authors declare that they have no known competing financial interests or personal relationships that could have appeared to influence the work reported in this paper.

Acknowledgments

This study was supported by the National Research Foundation of Korea (NRF) grant funded by the Korean government (MSIT) (NRF-2019R1A2C2084974).

References

[1] M. Mrazova, Advanced composite materials of the future in aerospace industry, Incas Bull. 5 (3) (2013) 139.

[2] N.A. Siddiqui, S.U. Khan, P.C. Ma, C.Y. Li, J.-K. Kim, Manufacturing and characterization of carbon fibre/epoxy composite prepregs containing carbon nanotubes, Composites A 42 (10) (2011) 1412–1420.

[3] J. Song, Q. Deng, C. Chen, D. Hu, Y. Li, Rebuilding of metal components with laser cladding forming, Appl. Surf. Sci. 252 (22) (2006) 7934–7940.

[4] A.V. Azarov, F.K. Antonov, M.V. Golubev, A.R. Khaziev, S.A. Ushanov, Composite 3D printing for the small size unmanned aerial vehicle structure, Composites B 169 (2019) 157–163.

[5] D. Deng, H. Murakawa, FEM prediction of buckling distortion induced by welding in thin plate panel structures, Comput. Mater. Sci. 43 (4) (2008) 591–607.
[6] P. Nali, E. Carrera, Accurate buckling analysis of composite layered plates with combined thermal and mechanical loadings, J. Therm. Stresses 36 (1) (2013) 1–18.
[7] C. Tao, T. Dai, Analyses of thermal buckling and secondary instability of post-buckled S-FGM plates with porosities based on a meshfree method, Appl. Math. Model. 89 (2020) 268–284.
[8] Z. Chen, Y.-B. Yi, K. Bao, J. Zhao, Numerical analysis of the coupling between frictionally excited thermoelastic instability and thermal buckling in automotive clutches, Proc. Inst. Mech. Eng. J 233 (1) (2019) 178–187.
[9] A. Rastgo, H. Shafie, A. Allahverdizadeh, Instability of curved beams made of functionally graded material under thermal loading, Int. J. Mech. Mater. Des. 2 (1–2) (2005) 117–128.
[10] H. Wu, J. Yang, S. Kitipornchai, Dynamic instability of functionally graded multilayer graphene nanocomposite beams in thermal environment, Compos. Struct. 162 (2017) 244–254.
[11] H. Babaei, M.R. Eslami, Nonlinear bending analysis of size-dependent FG porous microtubes in thermal environment based on modified couple stress theory, Mech. Based Des. Struct. Mach. (2020) 1–22.
[12] P. Talebizadehsardari, A. Eyvazian, M.G. Azandariani, T.N. Tran, D.K. Rajak, R.B. Mahani, Buckling analysis of smart beams based on higher order shear deformation theory and numerical method, Steel Compos. Struct. 35 (5) (2020) 635–640.
[13] Y. Zhang, X. Liu, J. Zhao, Influence of temperature change on column buckling of multiwalled carbon nanotubes, Phys. Lett. A 372 (10) (2008) 1676–1681.
[14] J. Yang, K. Liew, Y. Wu, S. Kitipornchai, Thermo-mechanical post-buckling of FGM cylindrical panels with temperature-dependent properties, Int. J. Solids Struct. 43 (2) (2006) 307–324.
[15] F. Ebrahimi, M.R. Barati, Temperature distribution effects on buckling behavior of smart heterogeneous nanosize plates based on nonlocal four-variable refined plate theory, Int. J. Smart Nano Mater. 7 (3) (2016) 119–143.
[16] W. Chen, P. Lin, L. Chen, Thermal buckling behavior of thick composite laminated plates under nonuniform temperature distribution, Comput. Struct. 41 (4) (1991) 637–645.
[17] W. Yu, K. Chung, S. Chan, Column buckling of structural bamboo, Eng. Struct. 25 (6) (2003) 755–768.
[18] M. Seif, B.W. Schafer, Local buckling of structural steel shapes, J. Construct. Steel Res. 66 (10) (2010) 1232–1247.
[19] J.H. Starnes Jr., R.T. Haftka, Preliminary design of composite wings for buckling, strength, and displacement constraints, J. Aircr. 16 (8) (1979) 564–570.
[20] K. Bakhti, M. Sekkal, E. Adda Bedia, A. Tounsi, Influence of material composition on buckling response of FG plates using a simple plate integral model, Smart Struct. Syst. 25 (4) (2020) 447–457.
[21] S. Natarajan, S. Chakraborty, M. Ganapathi, M. Subramanian, A parametric study on the buckling of functionally graded material plates with internal discontinuities using the partition of unity method, Eur. J. Mech. A Solids 44 (2014) 136–147.
[22] E. Farzaneh Joubaneh, A. Mojahedin, A. Khorshidvand, M. Jabbari, Thermal buckling analysis of porous circular plate with piezoelectric sensor-actuator layers under uniform thermal load, J. Sandwich Struct. Mater. 17 (1) (2015) 3–25.
[23] M. Khater, M. Eltaher, E. Abdel-Rahman, M. Yavuz, Surface and thermal load effects on the buckling of curved nanowires, Eng. Sci. Technol. Int. J. 17 (4) (2014) 279–283.
[24] B.S. Shariat, M. Eslami, Buckling of thick functionally graded plates under mechanical and thermal loads, Compos. Struct. 78 (3) (2007) 433–439.
[25] P. Jeyaraj, Buckling and free vibration behavior of an isotropic plate under nonuniform thermal load, Int. J. Struct. Stab. Dyn. 13 (03) (2013) 1250071.
[26] S. Janbaz, F. Bobbert, M. Mirzaali, A. Zadpoor, Ultra-programmable buckling-driven soft cellular mechanisms, Mater. Horiz. 6 (6) (2019) 1138–1147.
[27] D. Yang, B. Mosadegh, A. Ainla, B. Lee, F. Khashai, Z. Suo, K. Bertoldi, G.M. Whitesides, Buckling of elastomeric beams enables actuation of soft machines, Adv. Mater. 27 (41) (2015) 6323–6327.
[28] G. Wang, M. Li, J. Zhou, Modeling soft machines driven by buckling actuators, Int. J. Mech. Sci. 157 (2019) 662–667.
[29] D.W. Lee, J.H. Lee, J.-H. Jin, Innovative evolution of buckling structures for flexible electronics, Compos. Struct. 204 (2018) 487–499.
[30] L. Yin, R. Kumar, A. Karajic, L. Xie, J.-m. You, D. Joshuia, C.S. Lopez, J. Miller, J. Wang, From all-printed 2D patterns to free-standing 3D structures: Controlled buckling and selective bonding, Adv. Mater. Technol. 3 (5) (2018) 1800013.
[31] X. Hu, Y. Dou, J. Li, Z. Liu, Buckled structures: fabrication and applications in wearable electronics, Small 15 (32) (2019) 1804805.
[32] J.-H. Kang, H. Kim, C.D. Santangelo, R.C. Hayward, Enabling robust self-folding origami by pre-biasing vertex buckling direction, Adv. Mater. 31 (39) (2019) 0193006.
[33] Y. Shi, F. Zhang, K. Nan, X. Wang, J. Wang, Y. Zhang, Y. Zhang, H. Luan, K.-C. Hwang, Y. Huang, et al., Plasticity-induced origami for assembly of three dimensional metallic structures guided by compressive buckling, Extreme Mech. Lett. 11 (2017) 105–110.
[34] T.-U. Lee, X. Yang, J. Ma, Y. Chen, J.M. Gattas, Elastic buckling shape control of thin-walled cylinder using pre-embedded curved-crease origami patterns, Int. J. Mech. Sci. 151 (2019) 322–330.
[35] V.A. Bolaños Quiñones, H. Zhu, A.A. Solovev, Y. Mei, D.H. Gracias, Origami biosystems: 3D assembly methods for biomedical applications, Advanced Biosystems 2 (12) (2018) 1800230.
[36] H. Fu, K. Nan, W. Bai, W. Huang, K. Bai, L. Lu, C. Zhou, Y. Liu, F. Liu, J. Wang, et al., Morphable 3D mesostructures and microelectronic devices by multistable buckling mechanics, Nature Mater. 17 (3) (2018) 268–276.
[37] C. Wu, J. Fang, Q. Li, Multi-material topology optimization for thermal buckling criteria, Comput. Methods Appl. Mech. Engrg. 346 (2019) 1136–1155.
[38] S. Deng, K. Suresh, Topology optimization under thermo-elastic buckling, Struct. Multidiscip. Optim. 55 (5) (2017) 1759–1772.
[39] H.M. Lee, G.H. Yoon, Size optimization method for controlling the buckling mode shape and critical buckling temperature of composite structures, Compos. Struct. 255 (2021) 112902.
[40] K. Mehar, S.K. Panda, Y. Devarajan, G. Choubey, Numerical buckling analysis of graded CNT-reinforced composite sandwich shell structure under thermal loading, Compos. Struct. 216 (2019) 406–414.
[41] A. Schokker, S. Sridharan, A. Kasagi, Dynamic buckling of composite shells, Comput. Struct. 59 (1) (1996) 43–53.
[42] S. Panda, R. Natarajan, Analysis of laminated composite shell structures by finite element method, Comput. Struct. 14 (3–4) (1981) 225–230.